Available online at www.sciencedirect.com

ScienceDirect

Geochimica et Cosmochimica Acta 120 (2013) 65–79

Geochimica et Cosmochimica Acta

www.elsevier.com/locate/gca

An anoxic, Fe(II)-rich, U-poor ocean 3.46 billion years ago

Weiqiang Li [a,b,*], Andrew D. Czaja [a,b,c], Martin J. Van Kranendonk [d,e], Brian L. Beard [a,b], Eric E. Roden [a,b], Clark M. Johnson [a,b]

[a] University of Wisconsin-Madison, Department of Geoscience, 1215 West Dayton Street, Madison, WI 53706, United States
[b] NASA Astrobiology Institute, United States
[c] University of Cincinnati, Departments of Geology and Chemistry, 500 Geology-Physics Building, Cincinnati, OH 45221, United States
[d] Australian Center for Astrobiology and School of Biological, Earth and Environmental Sciences, University of New South Wales, Australia
[e] Australian Research Council Centre of Excellence for Core to Crust Fluid Systems and GEMOC, Department of Earth and Planetary Sciences, Macquarie University, Australia

Received 26 November 2012; accepted in revised form 25 June 2013; Available online 9 July 2013

Abstract

The oxidation state of the atmosphere and oceans on the early Earth remains controversial. Although it is accepted by many workers that the Archean atmosphere and ocean were anoxic, hematite in the 3.46 billion-year-old (Ga) Marble Bar Chert (MBC) from Pilbara Craton, NW Australia has figured prominently in arguments that the Paleoarchean atmosphere and ocean was fully oxygenated. In this study, we report the Fe isotope compositions and U concentrations of the MBC, and show that the samples have extreme heavy Fe isotope enrichment, where δ^{56}Fe values range between +1.5‰ and +2.6‰, the highest δ^{56}Fe values for bulk samples yet reported. The high δ^{56}Fe values of the MBC require very low levels of oxidation and, in addition, point to a Paleoarchean ocean that had high aqueous Fe(II) contents. A dispersion/reaction model indicates that O_2 contents in the photic zone of the ocean were less than 10^{-3} μM, which suggests that the ocean was essentially anoxic. An independent test of anoxic conditions is provided by U–Th–Pb isotope systematics, which show that U contents in the Paleoarchean ocean were likely below 0.02 ppb, two orders-of-magnitude lower than the modern ocean. Collectively, the Fe and U data indicate a reduced, Fe(II)-rich, U-poor environment in the Archean oceans at 3.46 billion years ago. Given the evidence for photosynthetic communities provided by broadly coeval stromatolites, these results suggests that an important photosynthetic pathway in the Paleoarchean oceans may have been anoxygenic photosynthetic Fe(II) oxidation.

1. INTRODUCTION

The evolution of photosynthesis was a critical evolutionary step in the history of life on Earth (e.g., Canfield, 2005). It has been proposed that anoxygenic photosynthesis preceded oxygenic photosynthesis (e.g., Hohmann-Marriott and Blankenship, 2011), in part because the Archean atmosphere and oceans of Earth are generally considered to have been anoxic, and also because anoxygenic photosynthesis is deeply rooted in the 16s rRNA tree of life (Xiong et al., 2000). The first rise in atmospheric oxygen, termed the "Great Oxidation Event" (GOE), has been proposed to have occurred between ~2.45 and 2.2 Ga (Holland, 1984, 2006). The GOE model was developed based on geologic occurrences of detrital pyrite, siderite, and uraninite in sediments deposited before the GOE, as well as retention of Fe in paleosols after the GOE (Holland, 1999), amongst other geological observations, although some workers have argued for a much earlier oxygenation of the atmosphere (e.g., Hoashi et al., 2009). Support for the GOE at ~2.4 Ga comes from the disappearance of mass-independent fractionation of S isotope after the GOE (Farquhar et al., 2000). Recent geochemical studies, however, increasingly provide evidence for a more complex evolution of

* Corresponding author at: University of Wisconsin-Madison, Department of Geoscience, 1215 West Dayton Street, Madison, WI 53706, United States. Tel.: +1 6087727386.
E-mail addresses: wli@geology.wisc.edu, liweiq@gmail.com (W. Li).

0016-7037/$ - see front matter © 2013 Elsevier Ltd. All rights reserved.
http://dx.doi.org/10.1016/j.gca.2013.06.033

atmospheric O_2 levels prior to the GOE as compared to a simple "step-function" (Anbar et al., 2007; Kaufman et al., 2007; Wille et al., 2007; Garvin et al., 2009; Godfrey and Falkowski, 2009; Ono et al., 2009; Duan et al., 2010; Kendall et al., 2010; Voegelin et al., 2010; Czaja et al., 2012; Reinhard et al., 2013).

Attempts to constrain the evolution of oxygenic photosynthesis have been controversial. For example, the timing of the evolution of oxygenic photosynthesis has been partially constrained to ~2.7 Ga, based on molecular biomarkers (Brocks et al., 1999; Eigenbrode and Freeman, 2006; Eigenbrode et al., 2008; Waldbauer et al., 2009), although this line of research has been highly controversial (e.g. Rasmussen et al., 2008). Large microfossils of 3.4–3.1 Ga age have been interpreted to be possible eukaryotes or possible cyanobacteria, which, if confirmed, would suggest an even earlier origin for oxygenic photosynthesis (Sugitani et al., 2007, 2010; Javaux et al., 2010). Other researchers point to geological evidence that may indicate stillearlier oxygenation of the atmosphere, and therefore, a very early appearance of oxygenic photosynthesis. For example, hematite in the 3.46 billion-year-old (Ga) Marble Bar Chert Member (MBC), and in the stratigraphically younger Apex Basalt, from Western Australia, has been interpreted to reflect an O_2-bearing Archean ocean and atmosphere in the Paleoarchean (Hoashi et al., 2009; Kato et al., 2009). Other workers have disagreed with an early timing of oxidation for the hematite-bearing Apex Basalt (Li et al., 2012).

In this study, we focus on the origin and paleo-environmental significance of hematite from the 3.46 Ga Marble Bar Chert Member (MBC) of the Duffer Formation, from the Pilbara Craton, Western Australia (Van Kranendonk et al., 2007b). Hoashi et al. (2009) interpreted hematite in the MBC to have precipitated from a fully-oxygenated Archean ocean at the time of deposition at 3.46 Ga, which in turn would suggest that oxygenic photosynthesis had evolved prior to that time. Alternatively, Van Kranendonk et al. (2008) suggested that hematite in jaspilitic chert from the conformably underlying ca. 3.48 Ga Dresser Formation formed as a result of alteration of primary siderite during circulation of high pH hydrothermal fluids. Here, we combine Fe isotopes, which can constrain the extent of oxidation, with U–Th–Pb isotopes, which provide an estimate of seawater U contents as an independent measure of oxygen abundance, and as a test for post-depositional alteration of the host rocks. Our results indicate that hematite in the MBC was precipitated by a very small extent of oxidation from an Fe(II)-rich, U-poor ocean at 3.46 Ga. We conclude that hematite in the 3.46 Ga MBC cannot be used to infer an origin for oxygenic photosynthesis prior to 3.5 Ga.

2. GEOLOGICAL BACKGROUNDS AND SAMPLES

The Marble Bar Chert Member (MBC) member of the ca. 3.46 Ga Duffer Formation is the most prominent chert unit in the Warrawoona Group, which is the lowest stratigraphic part of the well-preserved Pilbara Supergroup in the Paleoarchean Pilbara Craton in northwestern Australia (Van Kranendonk et al., 2002, 2007a) (Fig. 1). Thick successions of pillow basalts and finely bedded cherts within the Warrawoona Group indicate predominantly deep marine deposition (Van Kranendonk et al., 2007a). The MBC is generally 100–200 m thick, and extends north–south for over 120 km, west of the town of Marble Bar (Fig. 1). The depositional age of the MBC is well constrained to 3.46 Ga by U–Pb zircon geochronology on conformably underlying felsic volcanic rocks of the Duffer Formation (Fig. 1; Van Kranendonk et al., 2007b). A bedding-parallel shear zone that developed locally along the contact between the MBC and the overlying Apex Basalt (Kato et al., 2009) reflects the effects of tilting during tectonic deformation between 3.3 Ga and 2.9 Ga (Van Kranendonk et al., 2007a). The MBC and Apex Basalt at Marble Bar were buried to at least 3 km depth prior to 2.78 Ga, at which time they were uplifted, eroded, and overlain by rocks of the Fortescue Group. Phanerozoic uplift has once more exposed these rocks to the effects of recent weathering (Thorne, 2001; Van Kranendonk et al., 2007b).

Hematite-bearing chert layers (jasper) are abundant in outcrops of the MBC (Appendix 1; Van Kranendonk, 2006, 2010). Van Kranendonk (2006) interpreted the jasper layers to predate white chert within the MBC, as the latter occur as cross-cutting veins or *in situ* replacement of the hematite-bearing chert. However, the Australian continent has been exposed to deep weathering since the Triassic (Anand, 2005), which has produced weathering profiles that are commonly 50–100 m deep in Western Australia (Anand and Paine, 2002; Anand, 2005). A critical question, therefore, is the age of hematite formation in the MBC – is it early Archean, or could it be Neoarchean or even Phanerozoic?

The Archean Biosphere Drilling Project (ABDP) was initiated with the goal of obtaining samples below surface weathering zones, and the site for the first diamond drill core from this program (ABDP-1) is located about 4 km southwest of the town of Marble Bar (Fig. 1). The 260 m deep drill core of ABDP-1 intersects basalts of the 3.474–3.463 Ga Duffer Formation, the MBC, and the 3.46 Ga Apex Basalt (Fig. 1). There are abundant hematite-bearing bands in the drill core samples, even at depths greater than 100 m (Van Kranendonk, 2010).

The MBC samples analyzed in this study come from drill core depths of 169 m and 176 m in ABDP-1 (Figs. 1–3), and were sampled at the Geological Survey of Western Australia, Perth. These samples were analyzed for U–Th–Pb and Fe isotopes. In addition, we report new Fe isotope data for the Apex Basalt samples analyzed for U–Th–Pb isotopes by Li et al. (2012) from depths of 190–262 m, which have been variably oxidized. A non-oxidized basalt sample from the Duffer Formation at 42.6 m depth was also analyzed (Fig. 1).

3. ANALYTICAL METHODS

3.1. Sample preparation

Sampling of chert was undertaken using a thin (0.2 mm) diamond saw blade. For Fe isotope analysis, a small wedge-shaped piece 1 × 1 mm in size was cut from a quarter drill

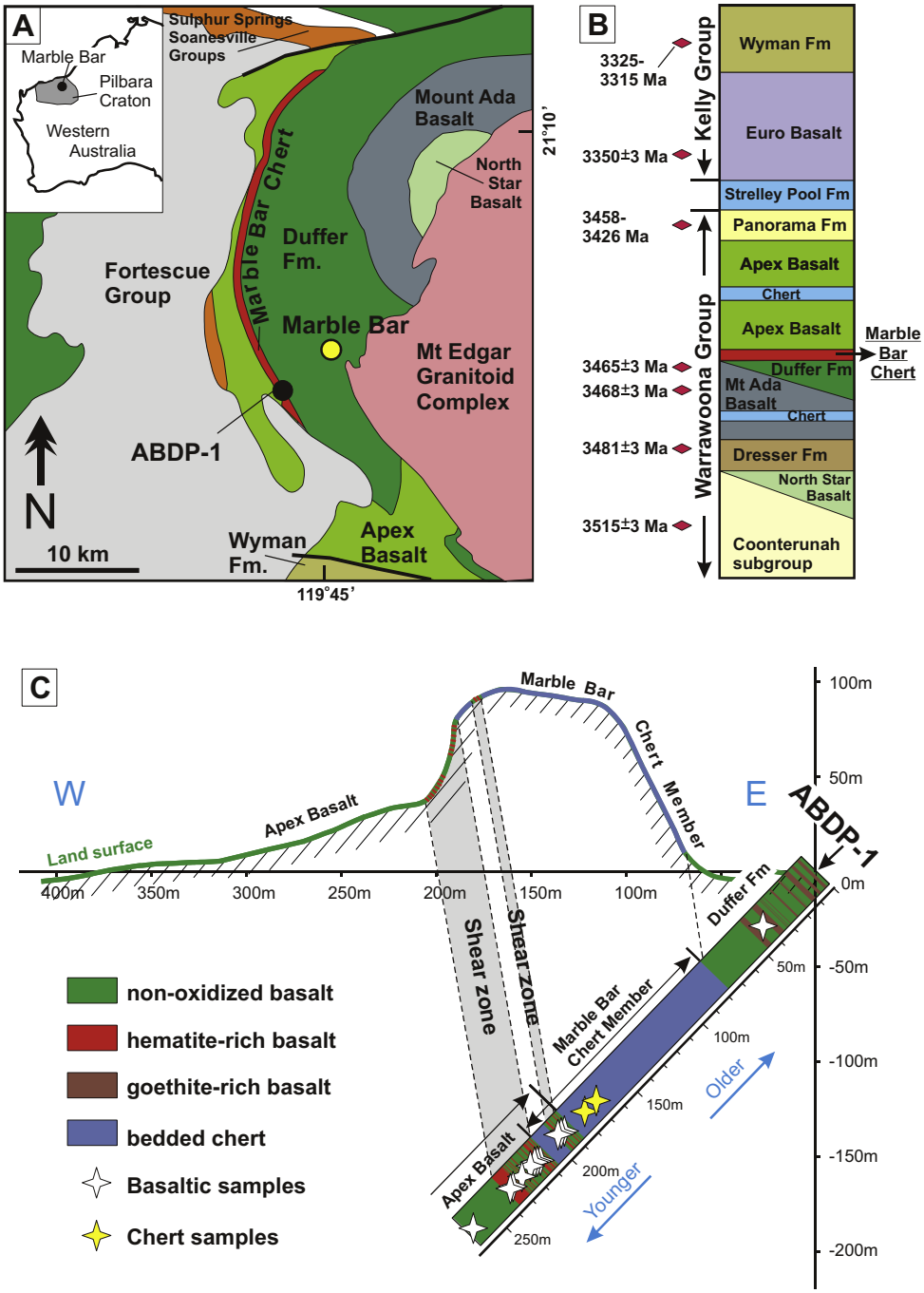

Fig. 1. Geological background of the samples analyzed in this study (after Li et al., 2012). Panel A shows geologic relations at Marble Bar and the location of the ABDP-1 drill core (modified from Hoashi et al., 2009 and Van Kranendonk et al., 2007a,b). Panel B shows the simplified stratigraphic column of the lower part of the Pilbara Supergroup, with ages constrained by zircon U–Pb geochronology (modified from Van Kranendonk et al., 2007b). Panel C shows a schematic cross section of the ABDP-1 drill core (modified from Kato et al., 2009).

core for each hematite-bearing red layer of the MBC (Figs. 2 and 3). For U–Th–Pb isotope analysis, a larger slab (cm size, >0.15 g) was cut because of the very low U and Th concentrations in chert samples. Both hematite-rich red layers and hematite-poor white layers of the MBC were sampled. Samples were examined under a binocular microscope before and after cutting in order to ensure that cracks, veins, and other secondary features were avoided. Samples were cleaned using acetone, 0.2 M HCl, and 18.2 MΩ H_2O in an ultrasonic bath for more than 10 min each to remove surface contamination, before being dried and weighed. This procedure ensured complete removal of any surface Fe, Pb and U contamination that may have been introduced during coring or sampling. Powder

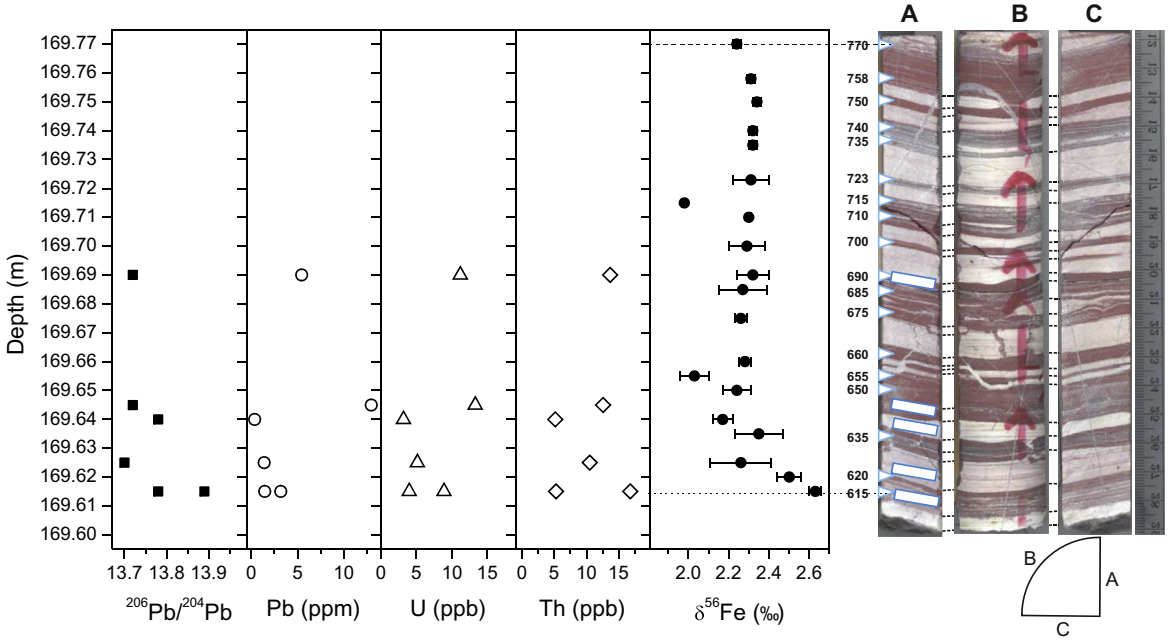

Fig. 2. Variation of Fe and U–Th–Pb isotope data along ABDP-1 drill core at a depth of 169.6–169.8 m. Blue triangles on core photo denote samples for Fe isotope analysis, and the adjacent small-font numbers denote depth in mm. Blue rectangles on core photo denote samples for U–Th–Pb isotope analysis. A, B, and C denote different sides of the quarter drill core. (For interpretation of the references to color in this figure legend, the reader is referred to the web version of this article.)

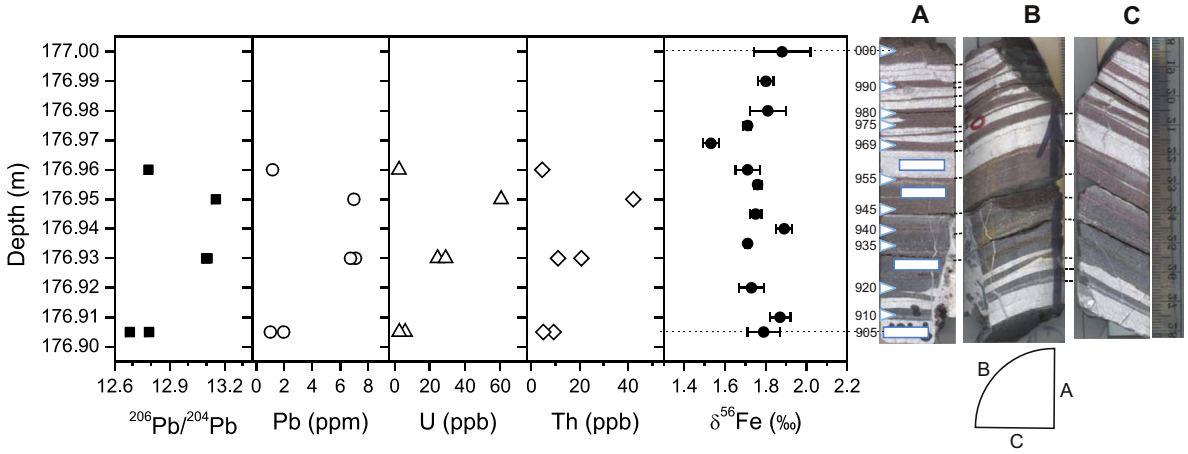

Fig. 3. Variation of Fe and U–Th–Pb isotope data along ABDP-1 drill core at a core depth of 176.9–177.0 m. Blue triangles on core photo denote samples for Fe isotope analysis, and the adjacent small-font numbers denote depth in mm. Blue rectangles on core photo denote samples for U–Th–Pb isotope analysis. A, B, and C denote different sides of the quarter drill core. (For interpretation of the references to colour in this figure legend, the reader is referred to the web version of this article.)

samples of Apex Basalt and Duffer Formation basalt that were analyzed for Fe isotope compositions were the same as those studied by Li et al. (2012), and sample preparation details may be found in that study.

Following the sample cleaning procedure noted above, sample digestion and ion-exchange chromatography were carried out in a clean room with HEPA-filtered air. Samples were digested using a mixture of double-distilled HF and Optima® grade HNO_3 in capped Savillex beakers that were heated overnight at 130 °C. Dissolved samples were converted to chloride form using double-distilled 8 M HCl and solutions were checked under a binocular microscope to ensure that the entire sample had dissolved and that no fluorides were present.

3.2. Iron isotope measurements

Prior to Fe isotope analysis, a small aliquot of each dissolved sample was taken for total Fe concentration measurement using the *Ferrozine* method (Stookey, 1970).

Approximately 100 μg of Fe from each sample was purified using anion-exchange resin (BioRad AG 1X4 200–400 mesh resin) and HCl (e.g., Beard et al., 2003). Iron solutions were diluted to 600 ppb and isotopic measurements were conducted using a Micromass *IsoProbe* MC-ICP-MS and an Aridus desolvating nebulizer that aspirated at ~50 μL/min. Mass spectrometry followed the procedures reported by Beard et al. (2003). Isotopic data are reported as $^{56}Fe/^{54}Fe$ and $^{57}Fe/^{54}Fe$ ratios in standard delta (δ) notation, in units of per mil (‰), and the average of igneous rocks as the standard reference reservoir (Beard et al., 2003):

$$\delta^{56}Fe = [(^{56}Fe/^{54}Fe)_{sample}/(^{56}Fe/^{54}Fe)_{standard} - 1] \times 1000 \quad (1)$$

and

$$\delta^{57}Fe = [(^{57}Fe/^{54}Fe)_{sample}/(^{57}Fe/^{54}Fe)_{standard} - 1] \times 1000 \quad (2)$$

Relative to the average of igneous rocks, the international Fe isotope standard IRMM-014 has a $\delta^{56}Fe$ value of −0.09‰ on this scale (Beard et al., 2003). The external long-term reproducibility (2-SD) for $\delta^{56}Fe$ measurements using this method is ±0.08‰, as determined from analysis of multiple in-house Fe standard solutions, and synthetic samples (Fe standard solutions doped with matrix elements) that were processed through the ion-exchange procedure together with drill core samples (Appendix 2).

3.3. U–Th–Pb isotope measurements

For U–Th–Pb isotope analysis, each digested sample was divided into two aliquots; one aliquot was used for Pb isotope analysis and the other was spiked with a mixed ^{235}U–^{229}Th–^{208}Pb tracer to determine U, Th, and Pb concentrations by isotope-dilution mass spectrometry. Solutions were chemically purified by anion-exchange chromatography, where initial cation separation was done using 0.6 M HBr, followed by extraction of Pb using 6 M HCl (Li et al., 2012). The U and Th in the 0.6 M HBr wash was purified using a second anion-exchange column using HNO_3, followed by HCl, to separate a combined U and Th cut from the rest of the sample (Li et al., 2012). Total procedural blanks for Pb chemistry was 50–80 pg, which was less than 0.1% of the amount of Pb in the samples. Total procedural blanks for Th and U were <50 pg, which is less than 10% of the amount of Th and U in the samples. Isotope-dilution analysis of Pb, U, and Th produced concentration uncertainties of <0.03%, <0.23%, and <0.08%, respectively.

Lead isotope ratios were determined on a VG Instruments *Sector 54* thermal ionization mass spectrometer using a static multi-collector routine and a ^{208}Pb ion signal of 1.7–2.0×10^{-11} A. Lead was loaded onto single Re filaments and run using the Si–gel H_3PO_4 technique. Lead isotope ratios were corrected for mass fractionation by +0.125% per amu, as constrained by long-term measurement of the $^{207}Pb/^{206}Pb$ ratio of NIST SRM-981 and the $^{208}Pb/^{206}Pb$ ratio of SRM-982. External precision of Pb isotope analysis was ±0.052% per amu (2 SD, $n = 30$), based on repeat measurement of SRM-981 and SRM-982 during the analytical session.

Isotopic ratios of $^{235}U/^{238}U$ and $^{229}Th/^{232}Th$ were simultaneously measured using a Micromass *IsoProbe* MC-ICP-MS and a 50 μl/min self-aspirating, concentric-flow nebulizer and an Aridus® desolvating nebulization system. Instrumental mass bias was corrected using a sample-standard bracketing technique, using mixtures of Ames Th mixed with NBL-114 natural U ($^{238}U/^{235}U = 137.88$) as bracketing standards. The samples were diluted to match the total ion intensity of the standards. There were no memory effects during analysis, as on-peak zero measurements of U and Th remained unchanged after washout between samples. Tailing effects were negligible, and correction for abundance sensitivity did not shift the results outside analytical error.

4. RESULTS

Iron isotope compositions and concentrations for MBC and basaltic samples, and Pb isotope compositions and U–Th–Pb concentrations for MBC samples, are given in Appendix 2. Iron and U–Th–Pb isotope data for MBC samples are correlated to drill cores in Figs. 2 and 3. Iron isotope compositions of the basaltic samples are plotted against Fe content, $Fe^{(III)}/Fe_{Total}$ and Fe/Th ratios in Fig. 4.

4.1. Iron isotope results

The MBC samples have very high $\delta^{56}Fe$ values, ranging between +1.53‰ and +2.63‰ (Figs. 2 and 3; Appendix 2), that define the upper limit of measured $\delta^{56}Fe$ values for bulk terrestrial samples. The $\delta^{56}Fe$ values of samples from a drill core depth of 169.6–169.8 m vary between +1.98‰ and +2.63‰ (Fig. 2). These are systematically higher than $\delta^{56}Fe$ values of samples from a drill core depth of 176.90–170.00 m (Fig. 3). There is a steadily decreasing trend in $\delta^{56}Fe$ values from +2.63‰ at 169.61 m to +2.03‰ at 169.65 m (Fig. 2), and an increase in $\delta^{56}Fe$ values from +1.53‰ at 176.97 m to +1.88‰ at 177 m (Fig. 3). Other than these relations, there is no significant variation in $\delta^{56}Fe$ values between layers (Table EA-1). There is no correlation between $\delta^{56}Fe$ values and Fe concentrations, nor between isotopic composition and color (red/black) of the hematite-bearing layers. It should be noted that the Fe isotope compositions of hematite-poor white layers are consistent with those of the hematite-rich (red) layers (Figs. 2 and 3), indicating that $\delta^{56}Fe$ values do not correlate with Fe contents.

In contrast to the MBC samples, basaltic samples from the ABDP-1 drill core have much lower $\delta^{56}Fe$ values, ranging between −0.40‰ and +0.66‰ (Fig. 4). The majority of these samples cluster around 0‰ and the weighted average $\delta^{56}Fe$ value for all basaltic samples is 0.00‰, equal to the average of igneous rocks (Beard et al., 2003). The $\delta^{56}Fe$ values of basaltic samples only become significantly variable as $Fe^{(III)}/Fe_{Total}$ ratios increase to >0.9 (Fig. 4). There is no correlation between the $\delta^{56}Fe$ values and total Fe concen-

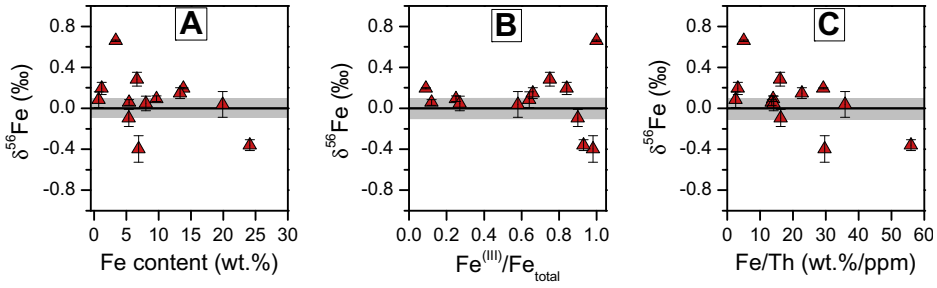

Fig. 4. Iron isotope composition of basaltic samples plotted against Fe content (A), $Fe^{(III)}/Fe_{total}$ ratios (B), and Fe/Th (C, in wt.%/ppm) ratios for Apex Basalt samples at Marble Bar (Li et al., 2012). The gray area denotes the $\delta^{56}Fe$ range of igneous rocks. (For interpretation of the references to colour in this figure legend, the reader is referred to the web version of this article.)

trations in the basalts, nor between $\delta^{56}Fe$ values and Fe/Th ratios (Fig. 4).

4.2. U–Th–Pb isotope results

Lead concentrations in the MBC samples vary between 0.37 and 12.95 ppm, U between 3 and 60 ppb, and Th between 4.5 and 42.23 ppb (Appendix 2). Concentrations of Pb, U, and Th are higher in the hematite-bearing red/black layers than in the hematite-poor, white layers (Figs. 2 and 3). Notably, concentrations of Pb, U, and Th in the MBC samples are systematically lower than those of the basaltic samples from the same drill core, which are 1–58 ppm for Pb, 80–1040 ppb for U, and 233–694 ppb for Th (Li et al., 2012). Importantly, U contents are much lower than those of modern oceanic sediments (0.306–4.889 ppm, global average 1.68 ppm; Plank and Langmuir, 1998). The MBC samples have very non-radiogenic Pb isotope compositions (low $^{206}Pb/^{204}Pb$, $^{207}Pb/^{204}Pb$ and $^{208}Pb/^{204}Pb$ ratios relative to average crust) that, in general, overlap those of basaltic samples from the ABDP-1 drill core. The $^{206}Pb/^{204}Pb$ ratios of samples from a drill core depth of 169.6–169.8 m vary between 13.699 and 13.891 (Fig. 2), which are systematically higher than the $^{206}Pb/^{204}Pb$ ratios of samples from a drill core depth of 176.90–170.00 m that vary between 12.684 and 13.153 (Figs. 2 and 3).

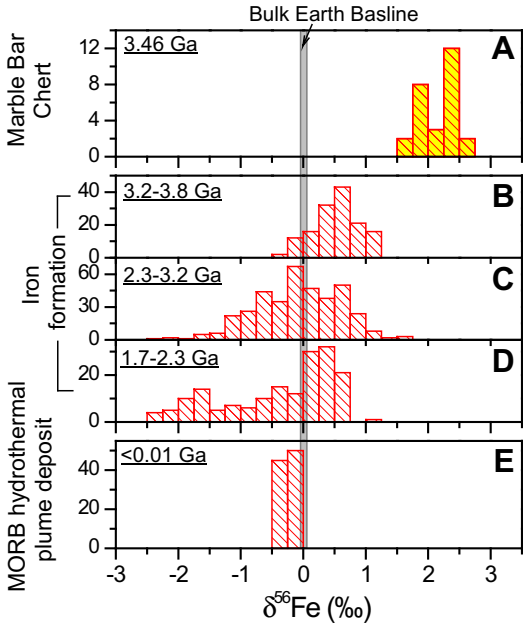

Fig. 5. Comparison of Fe isotope compositions of the MBC samples from the ABDP-1 drill core (part A, this study), Archean and Proterozoic iron formation (parts B–D, compiled from literature, data sources given in Appendix 4), and modern (<16 k yrs) hydrothermal plume precipitates from mid-ocean ridge environments (part E, Severmann et al., 2004).

5. DISCUSSION

5.1. Contrasting origin for hematite in the Marble Bar Chert and Apex Basalt

The hematite-bearing bands of the MBC have the highest $\delta^{56}Fe$ values ever reported from natural bulk rocks (Fig. 5). These contrast sharply with the igneous and near-igneous values (average $\delta^{56}Fe$ ~0‰; Beard et al., 2003) of variably oxidized samples of the Apex Basalt (Fig. 4). The large contrast in Fe isotope compositions between hematite in the MBC and that in the oxidized portions (hematite and goethite; Kato et al., 2009) of the Apex Basalt indicates distinct processes of formation.

The small variation in $\delta^{56}Fe$ values of the Apex Basalt (Fig. 4 and Table S1), averaging 0‰, suggests that Fe in Apex Basalt is primarily igneous in origin. The limited range in $\delta^{56}Fe$ values, which occurs only in the most oxidized samples, most likely reflects small extents of internal redistribution of Fe during oxidation. The fact that the two samples that have low $\delta^{56}Fe$ values also have high Fe/Th ratios, and that the samples with the highest $\delta^{56}Fe$ values also have low Fe/Th ratios (Fig. 4) implies that some samples might have released isotopically light Fe into fluids during weathering. This isotopically light Fe was then oxidized and re-precipitated, causing enrichment of isotopically light Fe oxides. Iron mobility could have been promoted by weathering of sulfides that were formed at 2.76 Ga at Marble Bar (Kato et al., 2009), which produced a locally acidic and redox-active environment that might enable small-scale Fe mobility and Fe isotope fractionation. Although Kato et al. (2009) suggest that oxidation occurred in the Archean, Li et al. (2012) documented Phanerozoic U mobility that correlated with the extent of oxidation,

indicating that oxidation of the Apex Basalt most likely occurred via channelized groundwater flow during deep Phanerozoic weathering. Under such conditions, large-scale Fe mobility would not be expected, and this is supported by the limited range in δ^{56}Fe values and the fact that the average δ^{56}Fe value lies at the value for igneous rocks.

In the MBC, the very high δ^{56}Fe values rule out the possibility that Fe was transported from the Apex Basalt. Moreover, the very high δ^{56}Fe values of the MBC are inconsistent with hematite formation by *in situ* oxidation of Fe(II)-bearing minerals such as siderite, as has been proposed for some jaspers in the underlying Dresser Formation (Van Kranendonk et al., 2008). Siderite that precipitated from an Archean ocean should have had a δ^{56}Fe value below $-0.5‰$ (Polyakov and Mineev, 2000; Wiesli et al., 2004; Johnson et al., 2008; Rustad et al., 2010), and *in situ* alteration to hematite should retain the negative δ^{56}Fe values. Furthermore, the low solubility of Fe(III) oxides and hydroxides at circumneutral pH (e.g., Kuma et al., 1996, and references therein) makes it unlikely that significant quantities of Fe could be leached from the MBC under oxidized conditions. We therefore conclude that the hematite in the MBC was *not* produced by the Phanerozoic oxidation event that oxidized the Apex Basalt at Marble Bar. This interpretation is consistent with the fracture and vein patterns in the drill core (Fig. 1C), that suggest groundwater movement was likely along channelized fracture systems.

5.2. Isotopic constraints of oxidation of Fe(II) in the Archean ocean

The likely source of aqueous Fe(II) that was oxidized to form hematite in the MBC was hydrothermal fluids, which should have had a δ^{56}Fe value of around $0‰$, or slightly negative (Yamaguchi et al., 2005; Johnson et al., 2008). Oxidation of aqueous Fe(II) in modern marine hydrothermal systems produces precipitates that have slightly negative δ^{56}Fe values (Fig. 5), reflecting essentially quantitative oxidation. The very high δ^{56}Fe values of hematite in the MBC, therefore, do not support a fully oxidized Archean ocean, as proposed by Hoashi et al. (2009). Rather, the very high δ^{56}Fe values can only be explained by *partial* oxidation of aqueous Fe(II), given the $\sim$3–4‰ fractionation in ^{56}Fe/^{54}Fe between oxides and aqueous Fe(II) (Wu et al., 2012).

Constraints on the extent of oxidation of aqueous Fe(II) in an Archean ocean can be made using a one-dimensional dispersion/reaction model, which assumes aqueous Fe(II) released from hydrothermal vents diffuses upwards to the photic zone, followed by oxidation of $Fe(II)_{aq}$ to Fe(III) hydroxides (Czaja et al., 2012, 2013). The limitation of the dispersion/reaction model is that it may not accurately describe upwelling of hydrothermal Fe(II), as the solution of the model relies on a steady-state condition of the ocean. Nevertheless, the dispersion/reaction model is superior compared with a simple Rayleigh fractionation model that is commonly used in geochemical studies, which is not an appropriate model for interpreting Fe isotope fractionation during oxidation in the photic zone because it is a closed-system model and does not account for a continual influx of $Fe(II)_{aq}$ and outflux of $Fe(OH)_3$ precipitates. Using the dispersion/reaction model of Czaja et al. (2012, 2013), we produced vertical profiles for concentrations and isotope compositions of $Fe(II)_{aq}$ and $Fe(OH)_3$, at different rates of $Fe(II)_{aq}$ oxidation (Appendix 3). In the model, oxidation could occur either anaerobically or aerobically, which simulates oxidation by either anoxygenic Fe(II)-oxidizing photosynthetic bacteria, or by free oxygen generated by oxygenic photosynthetic bacteria, respectively; in the latter case, our model can provide constraints on the amount of free oxygen that may have been present.

The dispersion/reaction model of Czaja et al. (2012, 2013) produces broadly similar profiles of concentrations and isotopic compositions of $Fe(II)_{aq}$ and $Fe(OH)_3$ over a wide range of input parameters (Appendix 3). Although many input parameters may be varied in the model, the most important factor that affects the results is the Fe(II) oxidation rate ($f_{\text{Fe-oxidation}}$). At a high rate of Fe(II) oxidation, which may be produced either by high O_2 from photosynthesis or by high activity of anoxygenic Fe(II)-oxidation, a low-$Fe(II)_{aq}$ zone is developed in the uppermost part of the photic zone. At such high rates of oxidation, the weighted average δ^{56}Fe value for $Fe(OH)_3$ is close to $0‰$ (Fig. 6; Appendix 3), reflecting quantitative Fe(II) oxidation of the Fe(II) hydrothermal input, assumed to have $\delta^{56}Fe = 0‰$. At lower Fe(II) oxidation rates, however, high $Fe(II)_{aq}$ concentrations develop in the photic zone, which in turn decreases the upwards $Fe(II)_{aq}$ flux ($f_{\text{Fe-transport}}$), as required to maintain a steady-state condition in the dispersion/reaction model ($f_{\text{Fe-transport}} = f_{\text{Fe-oxidation}}$). This relation occurs because the $Fe(II)_{aq}$ flux is a function of the $Fe(II)_{aq}$ concentration gradient in the water column and the eddy dispersion coefficient. Under these conditions, $Fe(II)_{aq}$ in the photic zone is partially oxidized, and the oxidation product, $Fe(OH)_3$ precipitates, has positive δ^{56}Fe values (Fig. 6; Appendix 3).

Dispersion/reaction modeling shows a rough linear relation between δ^{56}Fe values of Fe(III) hydroxides and the oxidation flux ($f_{\text{Fe-oxidation}}$) between zero and f_{ref}, a parameter defined as the maximum diffusive Fe(II) flux from the Fe(II) source to the photic zone ($f_{\text{ref}} = D \times \Delta C_{\text{ref}}/z_{\text{ref}}$; Kappler et al., 2005) (Fig. 6). D is the eddy dispersion coefficient, ΔC_{ref} is the Fe concentration difference between Fe(II) source and Fe-depleted zone ($C_{\text{Fe(II)-source}}$-0), and z_{ref} is the distance between the Fe(II) source and the bottom of the photic zone. The slope of the rough linear relation is dependent on the Fe isotope fractionation factor between aqueous Fe(II) and Fe(III) hydroxides (Fig. 6). At high rates of photosynthesis, complete depletion of Fe(II) develops in the top of the photic zone. In the case of anoxygenic photosynthesis, microbes are concentrated in the bottom of the photic zone and are limited by access to Fe(II). This is a scenario that has been proposed and discussed by Kappler et al. (2005) for anoxygenic photosynthetic oxidation of Fe(II). In the case of high oxygenic photosynthesis, complete depletion of Fe(II) also develops in the top of the photic zone at high rates of oxygen production, accompanied by a build-up of free O_2, which is transported downward in the water column to react with Fe(II) below the photic zone. It should be noted that $f_{\text{Fe-oxidation}}$ can be greater than

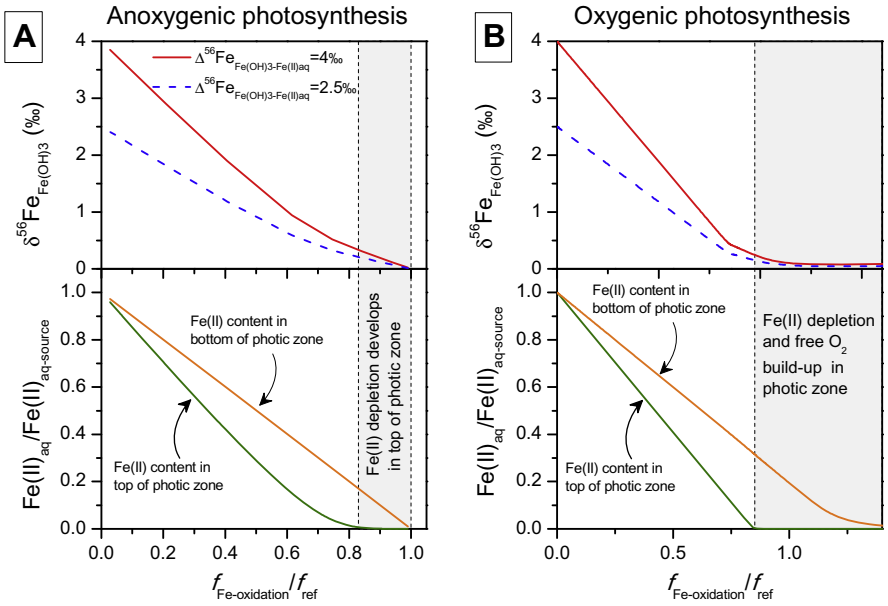

Fig. 6. Summary results of dispersion/reaction modeling of the Fe(II) oxidation at 3.46 Ga Marble Bar assuming Fe(II) oxidation by anoxygenic photosynthetic Fe(II) oxidizers (A), or by O_2 produced by oxygenic photosynthesis (B). $\Delta^{56}Fe_{Fe(OH)3\text{–}Fe(II)aq}$ is the Fe isotope fractionation factor between ferric hydroxides and aqueous Fe(II). Fe isotope composition of $Fe(OH)_3$ and Fe(II) concentrations at the top and bottom of photic zone are plotted against the $f_{Fe\text{-}oxidation}/f_{ref}$ ratio. $f_{Fe\text{-}oxidation}$ is the rate of Fe oxidation expressed as the flux of oxidized Fe that is settling as $Fe(OH)_3$, f_{ref} is the maximum flux of Fe(II) from the source to the bottom of photic zone by diffusion (for details, see Section 5.2). At low rates of Fe(II) oxidation, such as $f_{Fe\text{-}oxidation} < 0.8 f_{ref}$, the reducing capacity of Fe(II) provided by diffusion from the hydrothermal Fe(II) source dominates the photic zone, and even the top of photic zone contains significant amounts of aqueous Fe(II). As the Fe(II) oxidation rate increases, aqueous Fe(II) contents in the photic zone decrease, and eventually aqueous Fe(II) becomes depleted in the top of photic zone. With increasing activity of oxygenic photosynthesis, free O_2 begins to build up and the O_2-bearing water column expands downwards to below the photic zone, which increases the $f_{Fe\text{-}oxidation}$ by decreasing the diffusion distance of aqueous Fe(II) at a given depth from the Fe(II) source. The relations plotted in Fig. 6 were specifically chosen because they are insensitive to parameters and boundary conditions of the dispersion/reaction model. The most important parameters that determine the $\delta^{56}Fe$ values of Fe(III) hydroxide precipitates is the extent of oxidation and the $Fe(OH)_3$–$Fe(II)_{aq}$ Fe isotope fractionation factor.

f_{ref} and, in this case, free O_2 builds up and the oxygenated zone expands downwards to below photic zone, which decreases the diffusion distance of aqueous Fe(II) (Fig. 6B). In both cases (anoxygenic or oxygenic photosynthesis), close-to-zero $\delta^{56}Fe$ values for Fe(III) hydroxides are predicted, as Fe(II) is quantitatively oxidized.

The modeling results indicate that the $\delta^{56}Fe$ values of the ferric hydroxides/oxides may be used as a proxy for $Fe(II)_{aq}$ abundance in the photic zone. The high $\delta^{56}Fe$ values of the MBC iron oxides require a reduced, $Fe(II)_{aq}$-rich, photic zone. This, in turn, places constraints on permissible oxygen contents, which vary as a function of $\delta^{56}Fe$ values of $Fe(OH)_3$ precipitates (Fig. 7). Important variables are the $^{56}Fe/^{54}Fe$ fractionation factor between $Fe(OH)_3$ and $Fe(II)_{aq}$, and the depth of the basin, the latter of which exerts an influence on the rate of $Fe(OH)_3$ precipitation relative to $Fe(II)_{aq}$ influx. The small changes in $\delta^{56}Fe$ values in the MBC core may reflect subtle changes in extent of Fe(II) oxidation. The fact that the $\delta^{56}Fe$ values in a particular section of core do not correlate with Fe-rich or Fe-poor banding (Figs. 2 and 3) suggests that the variable Fe concentrations in MBC bands reflect variations in Fe(III) oxide accumulation rates (or SiO_2 precipitation rate) at the time of deposition, rather than changes in the extent of oxidation. In all cases, however, the O_2 contents esti-

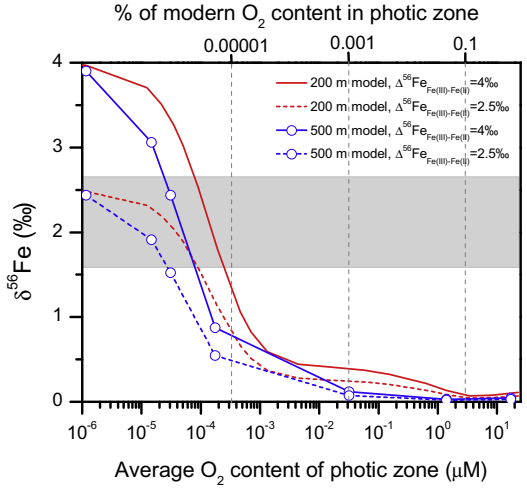

Fig. 7. Summary results of dispersion/reaction modeling showing the relation between average photic zone O_2 concentrations and the weighted average $\delta^{56}Fe$ values of the $Fe(OH)_3$ produced, assuming Fe(II) oxidation by O_2 produced by oxygenic photosynthesis. The curves represent results for Fe isotope fractionation factors ($\delta^{56}Fe_{Fe(OH)3\text{–}Fe(II)aq}$) of 4‰ and 2.5‰ in a 200 m basin and a 500 m basin. The shaded area represents the $\delta^{56}Fe$ value range measured in the MBC samples.

mated for the photic zone are less than 10^{-3} μM to produce the high measured δ^{56}Fe values, which is less than 0.0003% of modern O_2 contents in the photic zone. This conclusion is robust and is insensitive to changes in input parameters, including choice of $Fe(OH)_3$–$Fe(II)_{aq}$ Fe isotope fractionation factors, although the later parameter would be important if attempting to distinguish between O_2 contents of 10^{-3} to 10^{-6} μM (Fig. 7). For all practical purposes, however, all calculated O_2 contents of $<10^{-3}$ μM can be considered to indicate anoxic conditions in the photic zone, and this conclusion contrast greatly with the proposal of Hoashi et al. (2009) that the Fe oxides in the MBC reflect deposition in an oxygenated ocean.

5.3. U–Th–Pb isotope constraints on Archean ocean U contents

Uranium abundances in seawater will broadly correlate with oxygen contents because of the high solubility of U(VI) species relative to reduced species (Langmuir, 1978). Below we estimate the maximum seawater U contents of the Paleoarchean seawater from which the MBC precipitated, which provides an independent estimate for seawater oxygen contents relative to those based on Fe isotopes. Our approach is to estimate U contents using U–Th–Pb geochronology, which provides insights into changes due to radioactive decay and post-formation alteration. These issues are critical to assess in such ancient rocks because they bear on the confidence with which U can be used as a paleo-environmental proxy.

5.3.1. Post-depositional mobility of U and Pb in the MBC

It is possible that the low measured U contents in the MBC reflect post-depositional U loss through leaching by oxygenated groundwater circulation, but this can be critically evaluated using U–Th–Pb isotopes. The $^{206}Pb/^{204}Pb$–$^{208}Pb/^{204}Pb$–$^{207}Pb/^{204}Pb$ variations of the MBC indicate non-radiogenic isotope compositions, plotting along Pb–Pb arrays that correspond to low-$^{238}U/^{204}Pb$ ratios (μ) between 0 and 4 (Fig. 8), indicating long-term low U/Pb ratios. The MBC samples have Pb isotope compositions that overlap the basaltic samples in the ABDP-1 drill core, and lie between two Pb isotope end members (i.e., the non-radiogenic "ore lead" and the radiogenic "basalt lead") thatwere previously reported from the Warrawoona Group (Fig. 8: Li et al., 2012). On a $^{206}Pb/^{204}Pb$–$^{207}Pb/^{204}Pb$ plot, the MBC samples scatter about a line that has a slope equivalent to an age of 3435 ± 140 Ma and a MSWD of 2.9 (insert of Fig. 8B; best-fit line calculated using Isoplot v2.49 (Ludwig, 1999), where 2-σ errors for Pb isotope ratios are ±0.052%/amu). This age matches the depositional age of the MBC that is constrained by zircon U–Pb geochronology (Fig. 1). It is important to note, however, that all Pb reservoirs in the region liealong the isochron (Fig. 8), and therefore mixing relations will produce the same array (see discussion in Li et al., 2012). The MBC samples do not, however, plot on isochrons that correspond to a 3.46 Ga age on plots of $^{206}Pb/^{204}Pb$–$^{238}U/^{204}Pb$ and $^{208}Pb/^{204}Pb$–$^{232}Th/^{204}Pb$ (Fig. 9), indicating open-system behavior for the MBC samples.

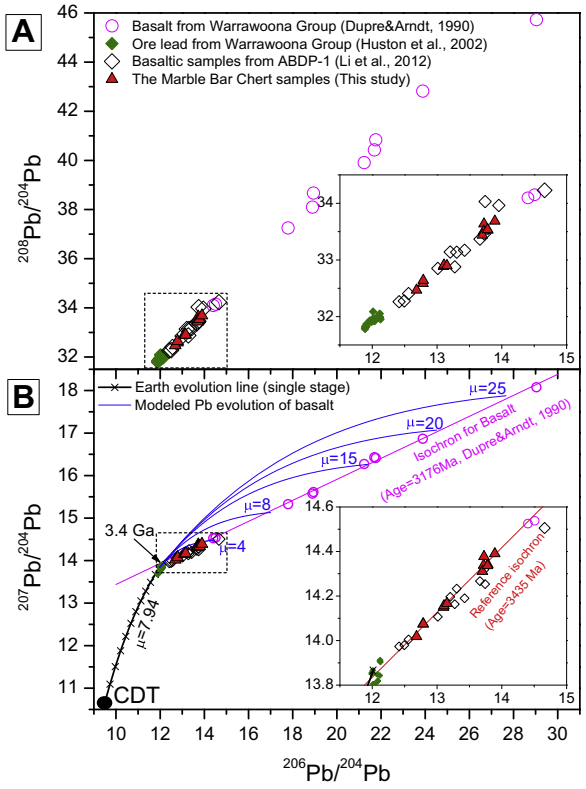

Fig. 8. $^{206}Pb/^{204}Pb$–$^{208}Pb/^{204}Pb$ (A) and $^{206}Pb/^{204}Pb$–$^{207}Pb/^{204}Pb$ (B) variations for the MBC samples (this study) and basaltic samples (Li et al., 2012) from the ABDP-1 drill core, the Warrawoona Group basalt samples near Marble Bar (Dupre and Arndt, 1990), and ore lead hosted in the Warrawoona Group (compiled by Huston et al., 2002). The details of the dashed box are shown in the insert in the lower-right corner of each diagram. For reference, a single-stage Pb growth curve for Earth is shown using an initial Pb isotope composition of Canon Diablo Troilite and$\mu_1 \approx 7.94$ (for detailed discussion, see Li et al., 2012). This Pb growth curve fits reasonably well with the ore lead isotope data from the Warrawoona Group, and intercepts the best-fitting isochrons for the basalts from Marble Bar at 3.46 Ga, which is the approximate formation age of these basalts. Secondary Pb growth curves were made using the Pb isotope composition of the primary Pb growth curve at 3.46 Ga as the starting point, and illustrated for μ_2 values between 4 and 25, the same range inferred for the basalts studied by Dupre and Arndt (1990); such a range in μ values matches that of primary (unaltered) basalts (White, 1993). By contrast, the μ_2 values for MBC and Apex Basalt samples from the ABDP-1 drill core are all below 4.

On a $^{208}Pb/^{204}Pb$–$^{232}Th/^{204}Pb$ diagram (Fig. 9B), all of the MBC chert samples plot to the left side of the reference isochron. Because Th should be relatively immobile, the very low $^{232}Th/^{204}Pb$ ratios likely reflect Pb addition, and the range of $^{208}Pb/^{204}Pb$ ratios can be explained as a mixture of low-$^{206}Pb/^{204}Pb$–$^{208}Pb/^{204}Pb$ "ore Pb" and high-$^{206}Pb/^{204}Pb$–$^{208}Pb/^{204}Pb$ "basalt Pb" components that have been added to the chert. The data relations on a $^{206}Pb/^{204}Pb$–$^{238}U/^{204}Pb$ diagram (Fig. 9A) are also consistent with Pb addition, although mobility of U is also possible, and is evaluated in Section 5.3.2 below. The isochron diagrams in Fig. 9A suggest that both the MBC and Apex

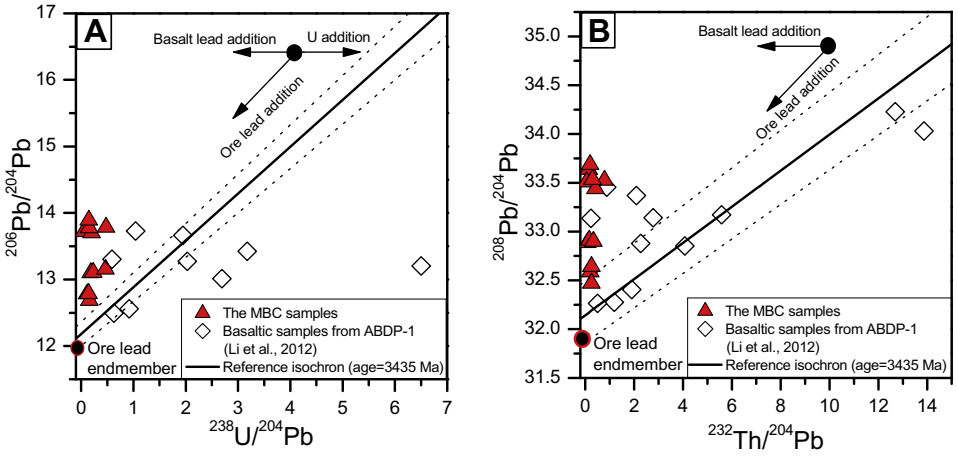

Fig. 9. $^{238}U/^{204}Pb$–$^{206}Pb/^{204}Pb$ (A) and $^{232}Th/^{204}Pb$–$^{207}Pb/^{204}Pb$ (B) variations for basalt samples from the ABDP-1 drill core. The reference isochron corresponds to an age of 3435 Ma (see insert, Fig. 8), and the dashed lines around the reference isochron represent an age uncertainty of ±140 Ma, as well as uncertainties in initial $^{206}Pb/^{204}Pb$ and $^{208}Pb/^{204}Pb$ ratios of ±0.18 and ±0.38, respectively (see Li et al., 2012 for details). The isotopic compositions of the "ore lead" end member are marked in the diagrams. The arrays in the plots show the trajectories a sample would take if influenced by addition of basalt Pb (Warrawoona basalts of Dupre and Arndt, 1990), addition of ore Pb (Warrawoona Group of Houston et al., 2002), or U addition.

Basalt have been influenced by the same event(s), as Pb addition has also been reported in the variably oxidized Apex Basalt (Li et al., 2012). Addition of "ore Pb" could have occurred at any time since 3.46 Ga because "ore Pb" defines the starting point of the $^{206}Pb/^{204}Pb$–$^{207}Pb/^{204}Pb$ "isochron" (see discussion in Li et al., 2012), whereas addition of "basalt lead" likely occurred recently, because the slope of the mixing trend on the $^{206}Pb/^{204}Pb$–$^{207}Pb/^{204}Pb$ diagram (Fig. 8B) represents an age that is consistent with the depositional age.

A key question is the effect of Pb addition to the U/Pb ratios, which is important to understand before U contents of the MBC at the time of deposition can be estimated. To account for the influence of Pb addition to the MBC, we evaluate the U/Pb ratios in the MBC by modeling the radiogenic decay of the primary depositional U component and compare the model results to measured results (Fig. 10). We assume a reference that represents samples that contained 5 ppm Pb with variable Pb isotope compositions ($\mu = 0.1$–3, $\kappa = 0.25$; for definitions of μ and κ, see Faure 1986), to approximate the measured Pb isotope compositions of the MBC samples, and these reference values define a family of lines in a $^{208}Pb/^{204}Pb$–$^{206}Pb/^{204}Pb$ plot (Fig. 10). The importance of incorporating $^{208}Pb/^{204}Pb$ ratios lies in the relative immobility of ^{232}Th, the parent to ^{208}Pb. We define U^*/Pb as the deviation in measured U/Pb ratios relative to those required to produce the least radiogenic Pb isotope ratios of the MBC. U^* could be viewed as "excess U" in the MBC at 3.46 Ga ago and it is further described mathematically in the following section (Section 5.3.2). Modeling results in Fig. 10 indicate that the Pb isotope deviations define a narrow range between 0 and +0.8% for U^*/Pb ratios. In contrast, if we assume that 3.46 Ga U contents were 100 or 300 ppb higher ($U^*/Pb = +2\%$ and +6%, respectively), but had recently decreased, the measured $^{206}Pb/^{204}Pb$–$^{208}Pb/^{204}Pb$ variations would have been highly skewed toward high $^{206}Pb/^{204}Pb$ ratios (Fig. 10), which is not observed. This conclusion is robust and independent of issues related to Pb addition, as U/Pb ratios are used in the model (Fig. 10). We cannot, however, rule out the possibility of U addition, a Phanerozoic event observed in the Apex Basalt adjacent to the MBC (Li et al., 2012). Therefore, the measured U contents in MBC samples ultimately will only constrain the upper limit of U contents in the MBC at the time of deposition at 3.46 Ga.

5.3.2. Estimating Archean seawater U concentration

A complete assessment of seawater U contents at the time of deposition of the MBC requires a mass-balance relation that accounts for four U components in the MBC samples: (1) U adsorbed by Fe(III) hydroxides during deposition in an Archean ocean ($U_{adsorbed}$) at 3.46 Ga, (2) an Archean detrital U component ($U_{detrital}$), (3) possible U added by a Phanerozoic event ($U_{Phanerozoic}$), and (4) the decrease in U contents of the Archean components due to ^{238}U and ^{235}U decay. The possibility of U addition in the Phanerozoic is based on the evidence presented by Li et al. (2012) for the Apex Basalt. Collectively, these terms may be described by the equation:

$$U_{measured} = U_{adsorbed} + U_{detrital} + U_{Phanerozoic} - U_{decay} \quad (3)$$

The detrital component of U can be constrained using the measured Th contents and a U/Th ratio of 0.25 that approximates that of average crust (Wignall and Myers, 1988; Chung and Chang, 1996; Fisher and Wignall, 2001). The amount of U decrease due to radioactive decay is calculated to be 47%, based on decay constants of ^{238}U and ^{235}U, present-day $^{238}U/^{235}U$ ratio, and an age of 3.46 Ga. The amount of U added during the Phanerozoic is difficult to constrain. An upper limit on U adsorbed, nevertheless, may be constrained by assuming $U_{Phanerozoic}$ is zero, although we postulate that the estimated $U_{adsorbed}$ content could be an order of magnitude lower than the upper

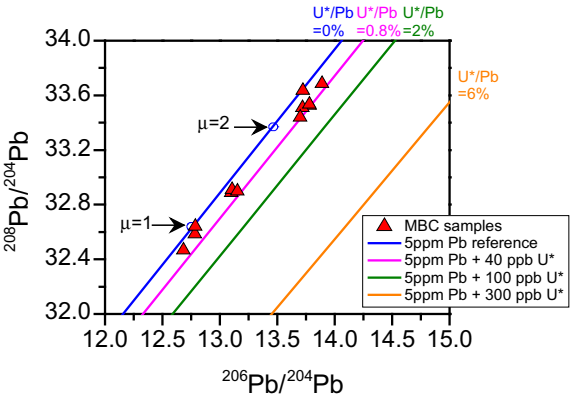

Fig. 10. $^{206}Pb/^{204}Pb$–$^{208}Pb/^{204}Pb$ diagram for the MBC and basalt samples from ABDP-1 drill core and modeling results. A line denotes a sample (or a set of samples) that has variable Pb isotope composition for a given U^*/Pb ratio.

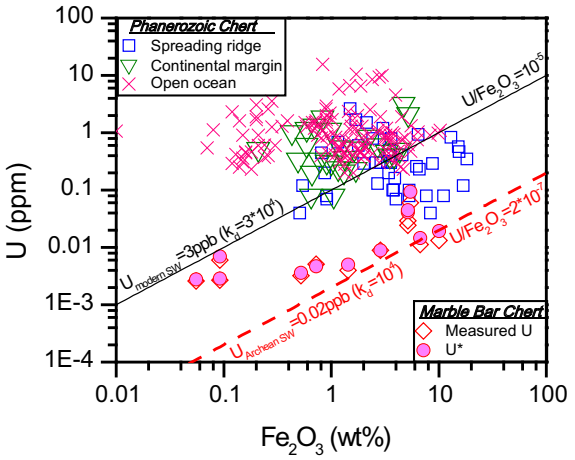

Fig. 11. A comparison of U and Fe_2O_3 contents between the Marble Bar Chert (MBC) samples and Phanerozoic cherts from three different tectonic settings. U^* is the upper limit of U in the MBC samples, calculated from the measured U–Th–Pb isotope systematics in the MBC, after correction for detrital contribution and U decay over time (see Section 5.3). Because of the possibility of Phanerozoic U addition (Li et al., 2012), we infer that the lower U/Fe_2O_3 curve most likely reflects the U contents of the primary precipitates at 3.46 Ga. Samples that scatter to the high U/Fe_2O_3 curve (upper curve) are most susceptible to U addition (see text), and hence likely over-estimate ancient seawater U contents. Data sources are given in Appendix 4.

bounds calculated here, given that Li et al. (2012) documented increases of up to 890% in the U/Th ratios of the ABDP-1 basalts during the Phanerozoic.

Uranium contents of seawater may be constrained using the $U_{adsorbed}$ calculated above, the iron oxide contents of the MBC, and data on U adsorption coefficients measured for iron oxides/hydroxides. Adsorption coefficients for U are very high for Fe(III) oxides and hydroxides, more than three-orders-of-magnitude higher than those for U adsorption to silicates, including SiO_2 phases (Waite et al., 1992), indicating that Fe(III) oxides/hydroxides should have controlled the U budget of the MBC. Partition coefficients (K_d) for U between Fe(III) hydroxide and aqueous solution are pH and pCO_2 dependent (Wazne et al., 2003; Davis et al., 2004). There is a general consensus that the pH value for Archean seawater was below that of the modern ocean, perhaps 7.5 or lower, based on expected higher atmospheric CO_2 contents (Walker, 1983; Grotzinger and Kasting, 1993; Ohmoto et al., 2004). Under these conditions, the U K_d between Fe(III) hydroxide and aqueous solution varies between 10^4 and 10^6 (Wazne et al., 2003; Davis et al., 2004). Using a conservative K_d of 10^4 and the U^*/Fe_2O_3 ratios of the MBC ($U^* = U_{measured} + U_{decay} - U_{detrital}$), upper limits for Archean seawater U contents during precipitation of the MBC are estimated at between 0.02 and 0.75 ppb (Fig. 11). Given the possibility of Phanerozoic U addition discussed above, such estimates are upper bounds and the seawater value at the time of deposition could be lower than 0.02 ppb U. We note that the highest inferred U^*/Fe_2O_3 values are those measured in samples that have the lowest Fe contents (Fig. 11), which suggests that the highest U contents inferred for Archean seawater are those samples that could be most susceptible to Phanerozoic U addition, given their low Fe contents. We therefore conclude that the U concentration of 3.46 Ga seawater was at least two orders of magnitude lower than that of modern seawater (3 ppb; see refs in Barnes and Cochran, 1990). Although there may be refinements that could be made to K_d estimates with new experimental data, we have chosen a conservative value. Uncertainties in the detrital component are less than 5%, given the narrow range in crustal U/Th ratios (e.g., Li et al., 2012).

Uranium occurs in primary igneous rocks as insoluble U(IV) compounds that, when oxidized, form highly soluble U(VI) species (Langmuir, 1978). The low redox potential of the U(VI)/U(IV) couple (0.27 V, Langmuir, 1978) makes U an element that is very sensitive to continental oxidation. The low U content in Archean seawater inferred here therefore complements geological evidence of detrital uraninite preservation in the Archean (Rasmussen and Buick, 1999), which attests to an anoxic Archean atmospheric and ocean conditions at 3.46 Ga. Such results are consistent with the implications of the high $\delta^{56}Fe$ values discussed above. Our results do not agree with the study by Rosing and Frei (2004), who argue for U-rich Archean seawater based on complex and partially reset Pb isotope compositions of 3.8 Ga metasedimentary rocks of the Isua Supracrustal Belt of southern West Greenland.

5.4. Implications for photosynthesis in the Archean ocean

The Fe isotope compositions of the MBC are consistent with the suggestion by Hoashi et al. (2009) that hematite in the MBC formed via oxidation of Fe(II) in the Archean ocean. Iron isotope data, however, rule out an oxygenated ocean as the cause of this Fe(II) oxidation, as proposed by these authors. Importantly, our modeling demonstrates that the occurrence of Fe(III) minerals cannot be taken as evidence for oxygenation of the atmosphere. There are several possible mechanisms for Fe(II) oxidation, including UV photo-oxidation, anaerobic photosynthetic Fe(II)-oxi-

dizing bacteria, or free oxygen produced by oxygenic photosynthesis. Although UV photo-oxidation of $Fe(II)_{aq}$ has been proposed as a mechanism for Fe(III) oxide precipitation in the Archean (Braterman et al., 1983), this is not supported by the experimental work of Konhauser et al. (2007), which demonstrated that UV photo-oxidation occurs at a rate much slower than the rate of precipitation of Fe(II) minerals such as greenalite and siderite under Archean seawater conditions (high dissolved silica, Fe(II), and high pCO_2). Although additional experimental work exploring a range of conditions may be required to fully rule out UV photo-oxidation, the evidence at hand suggests this is an unlikely process. Precipitation experiments indicate that siderite is isotopically lighter than aqueous Fe(II) by ca. 0.5‰ in δ^{56}Fe values (Wiesli et al., 2004), and greenalite probably also has low δ^{56}Fe values based on field studies (Frost et al., 2007); it is thus unlikely that hematite formed from these precursor minerals by oxidation or pH change (Garrels and Christ, 1965). Both reaction kinetics and Fe isotope compositions, therefore, rule out UV photo-oxidation as the origin of hematite in the MBC.

Remaining possible mechanisms for Fe(II) oxidation include oxidation by free oxygen, or by anaerobic photosynthetic Fe(II)-oxidizing bacteria. Under an anoxic Archean atmosphere, as suggested by a low seawater U concentration (this study) and occurrence of mass-independent fractionation of S isotopes at this time (Farquhar et al., 2007), any free oxygen would have been confined to localized "oxygen oases", such as might be associated with blooms of oxygenic photosynthesizing bacteria. Alternatively, anaerobic photoautotrophic microorganisms could have used Fe(II) rather than H_2O as an electron donor, producing Fe(III) rather than O_2 (Widdel et al., 1993). Experiments in systems that only contain Fe show that anaerobic photoautotrophic microorganisms produce hydrous ferric oxide as metabolic products that are enriched in heavy Fe isotopes by $\sim 1.5 \pm 0.2$‰ in δ^{56}Fe values relative to Fe(II) solutions (Croal et al., 2004), and Fe(II)-oxidizing nitrate-reducing bacteria may produce even larger fractionations of ~3‰ (Kappler et al., 2010). Co-precipitation of iron oxides with Si, as would be expected during formation of the MBC, produces further enrichment of heavy Fe isotopes due to bonding changes (Wu et al., 2012), where the Fe–Si hydroxide-$Fe(II)_{aq}$ fractionation factor can be as high as 4‰ in $^{56}Fe/^{54}Fe$. The Fe isotope compositions of the MBC, therefore, match well with these experimentally determined Fe isotope fractionations, and it can be reasonably concluded that anaerobic photosynthesis, in a Si-bearing system, could produce the measured δ^{56}Fe values for Fe(III) oxides in the MBC.

The very high δ^{56}Fe values require that the photic zone of Paleoarchean ocean was rich in Fe(II), the most important electron donor that could have supported anoxygenic photosynthesis (Canfield, 2005). We suggest that the combination of high-δ^{56}Fe values and low U contents could be a signature for anaerobic photosynthetic Fe(II)-oxidizing bacteria. Because anoxygenic photosynthesis is likely to be a deeply rooted metabolism (Blankenship, 1992; Hohmann-Marriott and Blankenship, 2011), and phylogenetic evidence suggests that oxygenic photosynthesis evolved after anoxygenic photosynthesis (Xiong et al., 2000), our results suggest that anoxygenic photosynthesis can be traced back to 3.46 Ga ago. Recent work by Czaja et al. (2013) on 3.8 Ga BIFs from the Isua Supracrustal Belt suggests that this metabolism may have been present even earlier, although the range in δ^{56}Fe values measured at Isua is less than that measured in the MBC.

Stromatolite-bearing units underlie and overlie the MBC in the Dresser Formation and Strelley Pool Formation, respectively (Allwood et al., 2006; Van Kranendonk, 2006), and have been interpreted to reflect precipitation by possible photosynthetic communities (Allwood et al., 2009). Tice and Lowe (2004) interpreted the 3.4 Ga Buck Reef Chert in the Barberton greenstone belt, South Africa, to preserve an anoxygenic photosynthetic community. Several studies have suggested that ~3.4 Ga photosynthetic communities likely used H_2 as an electron donor (Tice and Lowe, 2006; Bontognali et al., 2012). The isotopic results from the MBC add to evidence for a diversity of anoxygenic photosynthetic pathways in the Paleoarchean, where production of high-δ^{56}Fe oxides, in essentially anoxic environments, seems likely to indicate anoxygenic photosynthetic Fe(II) oxidation.

6. CONCLUSIONS

Hematite-bearing jaspilitic chert samples from the ABDP-1 drill core through the c. 3.46 Ga Marble Bar Chert Member of the Duffer Formation, Pilbara Craton, show extreme enrichment in heavy Fe isotopes ($\delta^{56}Fe = +1.53$‰ to $+2.63$‰), the highest δ^{56}Fe values reported from natural rocks. These results contrast with near-zero δ^{56}Fe values of the hematite-bearing Apex Basalt adjacent to the MBC, indicating that hematite in the MBC was not produced during the Phanerozoic event that oxidized the Apex Basalt. The very high δ^{56}Fe values can only be explained by partial oxidation in an Fe(II)-rich early Archean ocean (3.46 Ga). Dispersion/reaction modeling indicates that very low oxidation rates and low degrees of Fe(II) oxidation are needed to produce the highly positive δ^{56}Fe values. In particular, modeling strongly suggests that the photic zone of the 3.46 Ga ocean was reduced and buffered by excess Fe(II). In fact, modeling suggests that photic zone oxygen contents were less than 10^{-3} μM, less than 0.0003% of modern photic zone levels. Importantly, the dispersion/reaction modeling can more accurately determine the extent of oxidation and attendant levels of O_2, relative to more traditional modeling, such as simple Rayleigh fractionation, an approach that is not appropriate for a dynamic environment such as shallow marine settings.

The MBC samples contain ppb-levels of U and Th that are orders-of-magnitude lower than that of Phanerozoic cherts. The low Th contents indicate low detrital components in the MBC samples. U–Th–Pb isotope systematics indicate that the MBC has undergone post-depositional alteration that added external Pb components to the MBC, which is consistent with results obtained from the Apex Basalt (Li et al., 2012). Modeling of U–Pb isotope decay, however, indicates that the low U contents of the MBC cannot be explained by recent U loss, despite the evidence

for Pb mobility. Based on the U–Th–Pb isotope data, we constrain the upper limit of U concentration that was adsorbed by Fe(III) hydroxides during deposition of the MBC, from which we calculate an upper limit of U concentration in 3.46 Ga seawater at ~0.02 ppb, at least two orders of magnitude lower than the modern seawater value. Because U is mobile only when oxidized, the low U concentration in the MBC samples is an independent geochemical proxy that indicates an anoxic atmosphere in the Archean at 3.46 Ga. Our U–Th–Pb results also highlight the importance of determining the "age" of U in ancient sedimentary rocks when using U as a paleo-redox proxy, either through element abundances or mass-dependant isotope fractionations.

Collectively, the extreme enrichment in heavy Fe isotopes and low-U contents rule out the hypothesis that the Archean ocean was oxic (Hoashi et al., 2009). The MBC is laterally extensive (~120 km) and was precipitated in a deep marine environment, suggesting that the Fe(II)-rich, U-poor nature inferred for seawater at 3.46 Ga existed at least on a basinal scale. Our results provide additional support for a growing body of evidence for anoxic conditions at ~3.4 Ga, and additionally point to anoxygenic photosynthetic Fe(II) oxidation as a likely phototrophic pathway in the Paleoarchean. The results presented here do not support the presence of oxygenic photosynthesis as the mechanism of oxidation of Fe(II) in the MBC.

ACKNOWLEDGEMENTS

We thank Drs. Harilaos Tsikos and Vincent Busigny for constructive reviews of the manuscript, and Prof. Timothy Lyons for editorial handling and comments. This research was funded by the NASA Astrobiology Institute. This is contribution number 329 of the ARC Centre of Excellence for Core to Crust Fluid Systems.

APPENDIX A. SUPPLEMENTARY DATA

Supplementary data associated with this article can be found, in the online version, at http://dx.doi.org/10.1016/j.gca.2013.06.033.

REFERENCES

Allwood A. C., Walter M. R., Kamber B. S., Marshall C. P. and Burch I. W. (2006) Stromatolite reef from the Early Archaean era of Australia. *Nature* **441**, 714–718.

Allwood A. C., Grotzinger J. P., Knoll A. H., Burch I. W., Anderson M. S., Coleman M. L. and Kanik I. (2009) Controls on development and diversity of Early Archean stromatolites. *Proc. Natl. Acad. Sci.* **106**, 9548–9555.

Anand R. R. and Paine M. (2002) Regolith geology of the Yilgarn Craton, Western Australia: implications for exploration. *Aust. J. Earth Sci.* **49**, 3–162.

Anand R. R. (2005) Weathering history, landscape evolution and implications for exploration. In *Regolith Landscape Evolution Across Australia* (eds. R. R. Anand and P. de Broekert). Cooperative Research Centre for Landscape Environments and Mineral Exploration, Perth, pp. 2–40.

Anbar A. D., Duan Y., Lyons T. W., Arnold G. L., Kendall B., Creaser R. A., Kaufman A. J., Gordon G. W., Scott C., Garvin J. and Buick R. (2007) A whiff of oxygen before the Great Oxidation Event? *Science* **317**, 1903–1906.

Barnes C. E. and Cochran J. K. (1990) Uranium removal in oceanic sediments and the oceanic U balance. *Earth Planet. Sci. Lett.* **97**, 94–101.

Beard B. L., Johnson C. M., Skulan J. L., Nealson K. H., Cox L. and Sun H. (2003) Application of Fe isotopes to tracing the geochemical and biological cycling of Fe. *Chem. Geol.* **195**, 87–117.

Blankenship R. E. (1992) Origin and early evolution of photosynthesis. *Photosynth. Res.* **33**, 91–111.

Bontognali T. R. R., Sessions A. L., Allwood A. C., Fischer W. W., Grotzinger J. P., Summons R. E. and Eiler J. M. (2012) Sulfur isotopes of organic matter preserved in 3.45-billion-year-old stromatolites reveal microbial metabolism. *Proc. Natl. Acad. Sci.* **109**, 15146–15151.

Braterman P. S., Cairns-Smith A. G. and Sloper R. W. (1983) Photo-oxidation of hydrated Fe^{2+} significance for banded iron formations. *Nature* **303**, 163–164.

Brocks J. J., Logan G. A., Buick R. and Summons R. E. (1999) Archean molecular fossils and the early rise of eukaryotes. *Science* **285**, 1033–1036.

Canfield D. E. (2005) The early history of atmospheric oxygen: homage to Robert M. Garrels. *Annu. Rev. Earth Planet. Sci.* **33**, 1–36.

Chung Y. and Chang W. C. (1996) Uranium and thorium isotopes in marine sediments off northeastern Taiwan. *Mar. Geol.* **133**, 89–102.

Croal L. R., Johnson C. M., Beard B. L. and Newman D. K. (2004) Iron isotope fractionation by Fe(II)-oxidizing photoautotrophic bacteria. *Geochim. Cosmochim. Acta* **68**, 1227–1242.

Czaja A. D., Johnson C. M., Roden E. E., Beard B. L., Voegelin A. R., Nagler T. F., Beukes N. J. and Wille M. (2012) Evidence for free oxygen in the Neoarchean ocean based on coupled iron–molybdenum isotope fractionation. *Geochim. Cosmochim. Acta* **86**, 118–137.

Davis J. A., Meece D. E., Kohler M. and Curtis G. P. (2004) Approaches to surface complexation modeling of Uranium(VI) adsorption on aquifer sediments. *Geochim. Cosmochim. Acta* **68**, 3621–3641.

Duan Y., Anbar A. D., Arnold G. L., Lyons T. W., Gordon G. W. and Kendall B. (2010) Molybdenum isotope evidence for mild environmental oxygenation before the Great Oxidation Event. *Geochim. Cosmochim. Acta* **74**, 6655–6668.

Dupré B. and Arndt N. T. (1990) Pb isotopic compositions of Archean komatiites and sulfides. *Chemical Geology* **85**, 35–56.

Eigenbrode J. L. and Freeman K. H. (2006) Late Archean rise of aerobic microbial ecosystems. *Proc. Natl. Acad. Sci.* **103**, 15759–15764.

Eigenbrode J. L., Freeman K. H. and Summons R. E. (2008) Methylhopane biomarker hydrocarbons in Hamersley Province sediments provide evidence for Neoarchean aerobiosis. *Earth Planet. Sci. Lett.* **273**, 323–331.

Farquhar J., Bao H. and Thiemens M. (2000) Atmospheric influence of Earth's earliest sulfur cycle. *Science* **289**, 756–758.

Farquhar J., Peters M., Johnston D. T., Strauss H., Masterson A., Wiechert U. and Kaufman A. J. (2007) Isotopic evidence for Mesoarchaean anoxia and changing atmospheric sulphur chemistry. *Nature* **449**, 706–709.

Faure G. (1986) *Principles of Isotope Geology*. John Wiley & Sons, New York.

Fisher Q. J. and Wignall P. B. (2001) Palaeoenvironmental controls on the uranium distribution in an upper carboniferous black

shale (Gastrioceras listeri Marine Band) and associated strata; England. *Chem. Geol.* **175**, 605–621.

Frost C. D., Blanckenburg F. v., Schoenberg R., Frost B. R. and Swapp S. M. (2007) Preservation of Fe isotope heterogeneities during diagenesis and metamorphism of banded iron formation. *Contrib. Miner. Petrol.* **153**, 211–235.

Garrels R. M. and Christ C. L. (1965) *Solutions, Minerals and Equilibria*. Harper and Row, New York.

Garvin J., Buick R., Anbar A. D., Arnold G. L. and Kaufman A. J. (2009) Isotopic evidence for an aerobic nitrogen cycle in the latest Archean. *Science* **323**, 1045–1048.

Godfrey L. V. and Falkowski P. G. (2009) The cycling and redox state of nitrogen in the Archaean ocean. *Nat. Geosci.* **2**, 725–729.

Grotzinger J. P. and Kasting J. F. (1993) New constraints on Precambrian ocean composition. *J. Geol.* **101**, 235–243.

Hoashi M., Bevacqua D. C., Otake T., Watanabe Y., Hickman A. H., Utsunomiya S. and Ohmoto H. (2009) Primary haematite formation in an oxygenated sea 3.46 billion years ago. *Nat. Geosci.* **2**, 301–306.

Hohmann-Marriott M. F. and Blankenship R. E. (2011) Evolution of photosynthesis. *Annu. Rev. Plant Biol.* **62**, 515–548.

Holland H. D. (1984) *The Chemical Evolution of the Atmosphere and Oceans*. Princeton University Press.

Holland H. D. (1999) When did the Earth's atmosphere become oxic? A Reply. *Geochem. News* **100**, 20–22.

Holland H. D. (2006) The oxygenation of the atmosphere and oceans. *Philos. Trans. R. Soc. B: Biol. Sci.* **361**, 903–915.

Huston D. L., Sun S.-S., Blewett R., Hickman A. H., Kranendonk M. V., Phillips D., Baker D. and Brauhart C. (2002) The Timing of Mineralization in the Archean North Pilbara Terrain, Western Australia. *Economic Geology* **97**, 733–755.

Javaux E. J., Marshall C. P. and Bekker A. (2010) Organic-walled microfossils in 3.2-billion-year-old shallow-marine siliciclastic deposits. *Nature* **463**, 934–938.

Johnson C. M., Beard B. L. and Roden E. E. (2008) The iron isotope fingerprints of Redox and biogeochemical cycling in modern and ancient earth. *Annu. Rev. Earth Planet. Sci.* **36**, 457–493.

Kappler A., Pasquero C., Konhauser K. O. and Newman D. K. (2005) Deposition of banded iron formations by anoxygenic phototrophic Fe(II)-oxidizing bacteria. *Geology* **33**, 865–868.

Kappler A., Johnson C. M., Crosby H. A., Beard B. L. and Newman D. K. (2010) Evidence for equilibrium iron isotope fractionation by nitrate-reducing iron(II)-oxidizing bacteria. *Geochim. Cosmochim. Acta* **74**, 2826–2842.

Kato Y., Suzuki K., Nakamura K., Hickman A. H., Nedachi M., Kusakabe M., Bevacqua D. C. and Ohmoto H. (2009) Hematite formation by oxygenated groundwater more than 2.76 billion years ago. *Earth Planet. Sci. Lett.* **278**, 40–49.

Kaufman A. J., Johnston D. T., Farquhar J., Masterson A. L., Lyons T. W., Bates S., Anbar A. D., Arnold G. L., Garvin J. and Buick R. (2007) Late Archean biospheric oxygenation and atmospheric evolution. *Science* **317**, 1900–1903.

Kendall B., Reinhard C. T., Lyons T. W., Kaufman A. J., Poulton S. W. and Anbar A. D. (2010) Pervasive oxygenation along late Archaean ocean margins. *Nat. Geosci.* **3**, 647–652.

Konhauser K. O., Amskold L., Lalonde S. V., Posth N. R., Kappler A. and Anbar A. (2007) Decoupling photochemical Fe(II) oxidation from shallow-water BIF deposition. *Earth Planet. Sci. Lett.* **258**, 87–100.

Kuma K., Nishioka J. and Matsunaga K. (1996) Controls on iron(III) hydroxide solubility in seawater: the influence of pH and natural organic chelators. *Limnol. Oceanogr.* **41**, 396–407.

Langmuir D. (1978) Uranium solution-mineral equilibria at low temperatures with applications to sedimentary ore deposits. *Geochim. Cosmochim. Acta* **42**, 547–569.

Li W., Johnson C. M. and Beard B. L. (2012) U–Th–Pb isotope data indicate Phanerozoic age for oxidation of the 3.4 Ga Apex Basalt. *Earth Planet. Sci. Lett.* **319–320**, 197–206.

Ludwig, K.R., (1999). Using Isoplot/Ex, Version 2.01: a geochronological toolkit for Microsoft Excel. Berkeley Geochronology Center Special Publication 1a, 1-47.

Ohmoto H., Watanabe Y. and Kumazawa K. (2004) Evidence from massive siderite beds for a CO_2-rich atmosphere before ~1.8 billion years ago. *Nature* **429**, 395–399.

Ono S., Kaufman A. J., Farquhar J., Sumner D. Y. and Beukes N. J. (2009) Lithofacies control on multiple-sulfur isotope records and Neoarchean sulfur cycles. *Precambr. Res.* **169**, 58–67.

Plank T. and Langmuir C. H. (1998) The chemical composition of subducting sediment and its consequences for the crust and mantle. *Chem. Geol.* **145**, 325–394.

Polyakov V. B. and Mineev S. D. (2000) The use of Mossbauer spectroscopy in stable isotope geochemistry. *Geochim. Cosmochim. Acta* **64**, 849–865.

Rasmussen B. and Buick R. (1999) Redox state of the Archean atmosphere: evidence from detrital heavy minerals in ca. 3250–2750 Ma sandstones from the Pilbara Craton, Australia. *Geology* **27**, 115–118.

Rasmussen B., Fletcher I. R., Brocks J. J. and Kilburn M. R. (2008) Reassessing the first appearance of eukaryotes and cyanobacteria. *Nature* **455**, 1101–1104.

Reinhard C. T., Planavsky N. J. and Lyons T. W. (2013) Long-term sedimentary recycling of rare sulphur isotope anomalies. *Nature* **497**, 100–103.

Rosing M. T. and Frei R. (2004) U-rich Archaean sea–floor sediments from Greenland – indications of >3700 Ma oxygenic photosynthesis. *Earth Planet. Sci. Lett.* **217**, 237–244.

Rustad J. R., Casey W. H., Yin Q.-Z., Bylaska E. J., Felmy A. R., Bogatko S. A., Jackson V. E. and Dixon D. A. (2010) Isotopic fractionation of Mg^{2+}(aq), Ca^{2+}(aq), and Fe^{2+}(aq) with carbonate minerals. *Geochim. Cosmochim. Acta* **74**, 6301–6323.

Severmann S., Johnson C. M., Beard B. L., German C. R., Edmonds H. N., Chiba H. and Green D. R. H. (2004) The effect of plume processes on the Fe isotope composition of hydrothermally derived Fe in the deep ocean as inferred from the Rainbow vent site, Mid-Atlantic Ridge, 36°14′N. *Earth Planet. Sci. Lett.* **225**, 63–76.

Stookey L. L. (1970) Ferrozine – a new spectrophotometric reagent for iron. *Anal. Chem.* **42**, 779–781.

Sugitani K., Grey K., Allwood A., Nagaoka T., Mimura K., Minami M., Marshall C. P., Van Kranendonk M. J. and Walter M. R. (2007) Diverse microstructures from Archaean chert from the Mount Goldsworthy–Mount Grant area, Pilbara Craton, Western Australia: Microfossils, dubiofossils, or pseudofossils? *Precambr. Res.* **158**, 228–262.

Sugitani K., Lepot K., Nagaoka T., Mimura K., Van Kranendonk M. J., Oehler D. Z. and Walter M. R. (2010) Biogenicity of morphologically diverse carbonaceous microstructures from the ca. 3400 Ma strelley pool formation, in the Pilbara Craton, Western Australia. *Astrobiology* **10**, 899–900.

Thorne A. M. (2001) Geology of the Fortescue Group, Pilbara Craton, Western Australia, Geological Survey of Western Australia Bulletin 114, Perth.

Tice M. M. and Lowe D. R. (2004) Photosynthetic microbial mats in the 3,416-Myr-old ocean. *Nature* **431**, 549–552.

Tice M. M. and Lowe D. R. (2006) Hydrogen-based carbon fixation in the earliest known photosynthetic organisms. *Geology* **34**, 37–40.

Van Kranendonk M. J., Hickman A. H., Smithies R. H., Nelson D. R. and Pike G. (2002) Geology and tectonic evolution of the Archean North Pilbara Terrain, Pilbara Craton, Western Australia. *Econ. Geol.* **97**, 695–732.

Van Kranendonk M. J. (2006) Volcanic degassing, hydrothermal circulation and the flourishing of early life on Earth: a review of the evidence from c. 3490–3240 Ma rocks of the Pilbara Supergroup, Pilbara Craton, Western Australia. *Earth-Sci. Rev.* **74**, 197–240.

VanKranendonk M. J., Smithies R. H., Hickman A. H. and Champion D. C. (2007a) Paleoarchean Development of a Continental Nucleus: the East Pilbara Terrane of the Pilbara Craton, Western Australia. In *Developments in Precambrian Geology* (eds. M. J. van Kranendonk, R. H. Smithies and V. C. Bennett). Elsevier, pp. 307–337, Chapter 4.1.

Van Kranendonk M. J., Smithies R. H., Hickman A. H. and Champion D. C. (2007b) Review: secular tectonic evolution of Archean continental crust: interplay between horizontal and vertical processes in the formation of the Pilbara Craton, Australia. *Terra Nova* **19**, 1–38.

Van Kranendonk M. J., Philippot P., Lepot K., Bodorkos S. and Pirajno F. (2008) Geological setting of Earth's oldest fossils in the ca. 3.5 Ga Dresser Formation, Pilbara Craton, Western Australia. *Precambr. Res.* **167**, 93–124.

Van Kranendonk M. J. (2010) *Fifth International Archean Symposium: Handbook for Archean drillcore at the GSWA core library*. Geological Survey of Western Australia.

Voegelin A. R., Nagler T. F., Beukes N. J. and Lacassie J. P. (2010) Molybdenum isotopes in late Archean carbonate rocks: implications for early Earth oxygenation. *Precambr. Res.* **182**, 70–82.

Waite T. D., Payne T. E., Davis J. A. and Sekine K. (1992) Alligators Rivers Analogue Project. Final Report Volume 13. Uranium Sorption. ISBN 0-642-599394.

Waldbauer J. R., Sherman L. S., Sumner D. Y. and Summons R. E. (2009) Late Archean molecular fossils from the Transvaal Supergroup record the antiquity of microbial diversity and aerobiosis. *Precambr. Res.* **169**, 28–47.

Walker J. C. G. (1983) Possible limits on the composition of the Archaean ocean. *Nature* **302**, 518–520.

Wazne M., Korfiatis G. P. and Meng X. (2003) Carbonate effects on hexavalent uranium adsorption by iron oxyhydroxide. *Environ. Sci. Technol.* **37**, 3619–3624.

Widdel F., Schnell S., Heising S., Ehrenreich A., Assmus B. and Schink B. (1993) Ferrous iron oxidation by anoxygenic phototrophic bacteria. *Nature* **362**, 834–836.

Wiesli R. A., Beard B. L. and Johnson C. M. (2004) Experimental determination of Fe isotope fractionation between aqueous Fe(II), siderite and "green rust" in abiotic systems. *Chem. Geol.* **211**, 343–362.

Wignall P. B. and Myers K. J. (1988) Interpreting benthic oxygen levels in mudrocks: a new approach. *Geology* **16**, 452–455.

Wille M., Kramers J. D., Nagler T. F., Beukes N. J., Schroder S., Meisel T., Lacassie J. P. and Voegelin A. R. (2007) Evidence for a gradual rise of oxygen between 2.6 and 2.5 Ga from Mo isotopes and Re-PGE signatures in shales. *Geochim. Cosmochim. Acta* **71**, 2417–2435.

Wu L., Percak-Dennett E. M., Beard B. L., Roden E. E. and Johnson C. M. (2012) Stable iron isotope fractionation between aqueous Fe(II) and model Archean ocean Fe–Si coprecipitates and implications for iron isotope variations in the ancient rock record. *Geochim. Cosmochim. Acta* **84**, 14–28.

Xiong J., Fischer W. M., Inoue K., Nakahara M. and Bauer C. E. (2000) Molecular evidence for the early evolution of photosynthesis. *Science* **289**, 1724–1730.

Yamaguchi K. E., Johnson C. M., Beard B. L. and Ohmoto H. (2005) Biogeochemical cycling of iron in the Archean–Paleoproterozoic Earth: constraints from iron isotope variations in sedimentary rocks from the Kaapvaal and Pilbara Cratons. *Chem. Geol.* **218**, 135–169.

Associate editor: Timothy Lyons